Chinese Chemical Letters 35 (2024) 109059

Contents lists available at ScienceDirect

Chinese Chemical Letters

journal homepage: www.elsevier.com/locate/cclet

Flexible electrochemical capacitor based NiMoSSe electrode material with superior cycling and structural stability

Jingxuan Liu, Shiqi Zhao, Xiang Wu*

School of Materials Science and Engineering, Shenyang University of Technology, Shenyang 110870, China

ARTICLE INFO

Article history:
Received 31 July 2023
Revised 23 August 2023
Accepted 6 September 2023
Available online 7 September 2023

Keywords:
Supercapacitors
NiMoSSe
Energy density
Power density
Cycling life

ABSTRACT

Constructing composited electrode material is considered to be an efficient strategy to improve their electrochemical performance. It can accelerate the charge transfer speed of ions and enhance the conductivity of electrode. Meanwhile, the formation of the hybrid structure can largely avoid the aggregation of two dimensional materials and increase the electrochemical active area of the electrode. In this work, we synthesize NiMoSSe electrode materials on nickel foam by a facile hydrothermal avenue. The prepared composite shows a specific capacitance of 1035 C/g at 1 A/g due to the synergistic effect between MoS_2 and $MoSe_2$ phases. In addition, the devices are assembled with NiMoSSe samples, which offers an energy density of 82.71 Wh/kg at a power density of 2700 W/kg.

To achieve the goal of sustainable energy sources development in the interim of this century, people are committed to seeking for some advanced energy storage and conversion technologies [1–5]. Among them, supercapacitors play an important role due to high power density and fast charging and discharging speed [6–9]. However, it cannot compete with traditional batteries owing to their low energy density [10,11]. It is necessary to design novel electrode materials with high capacitance and conductivity. MoS_2 material are widely studied as a typical 2D transition metal sulfide [12–14]. According to the arrangement of S atomic layer, it is usually divided into three phases: 1T, 2H and 3R [15]. 1T-MoS_2 structure is much suitable as the electrode material of supercapacitors because its large interlayer spacing [16]. However, it is easy to transform into thermodynamically stable 2H phase due to its high aging speed [17]. In addition, MoS_2 electrodes possess many oxidation states, which show large potential in pseudo-capacitors. Mishra *et al.* synthesized 2H-MoS_2 nano-flowers, which delivered a specific capacitance of 382 F/g at 1 A/g [18] MoS_2 material presents the theoretical capacity of 1403 F/g, but it is challenging to obtain this value because of its low crystallinity and limited conductivity.

$MoSe_2$ with Se-Mo-Se sandwich structure possesses larger interlayer spacing and better conductivity than MoS_2 electrodes [19,20]. It provides abundant active sites during Faraday redox reaction owing to its unique lamellar structure and surface characteristics [21,22]. In the previous reports, Vattikuti *et al.* prepared the leaf-like mesoporous $MoSe_2$ samples, which showed a capacitance of 257.38 F/g at 1 A/g [23]. However, layered $MoSe_2$ nanosheets are easy to aggregate due to van der Waals force, resulting in serious capacity attenuation [24]. To solve the above problems, Wang's group synthesized the $MoSe_2/MoS_2$ heterostructure with a specific capacitance of 1229.6 F/g at 1 A/g [25]. And the capacitance retention rate is 92.8% after 2000 cycles. The results prove that $MoSe_2$ materials possess intensive sulfur affinity and can effectively adsorb sulfides to form S-Mo-Se bonds.

In this work, we prepare NiMoSSe electrode materials by a simple hydrothermal route. The synergistic effect between $MoSe_2$ and MoS_2 electrodes ensures the formation of high-quality heterogeneous interfaces and greatly improves the specific capacitance of the materials. The as-obtained product delivers a specific capacitance of 1035 C/g at 1 A/g. It maintains 79.86% of the initial capacitance after 10000 cycles. The assembled asymmetric device presents an energy density of 82.71 Wh/kg at 2700 W/kg. The retention rate is 88.21% after 10000 times cycling.

Before the experiments, a piece of nickel foam (3×4 cm^2) was washed repeatedly with ethanol and deionized water, respectively. Then 1 mmol $Na_2MoO_4 \cdot 2H_2O$, x (x = 0, 1, 2) mmol Se powder, (2-x) mmol thiourea were dissolved into the mixed solution of 30 mL deionized water and 10 mL $N_2H_4 \cdot H_2O$. After that, the pretreated nickel foam was transferred to the above solution and heated at 180 °C for 18 h in a 100 mL autoclave. The corresponding samples were denoted as NiMoS, NiMoSSe and NiMoSe, respectively. For comparison, pure MoS_2, MoSSe and $MoSe_2$ powder were also fabricated without Ni foam under the same condition.

* Corresponding author.
E-mail addresses: wuxiang05@163.com, wuxiang05@sut.edu.cn (X. Wu).

https://doi.org/10.1016/j.cclet.2023.109059
1001-8417/

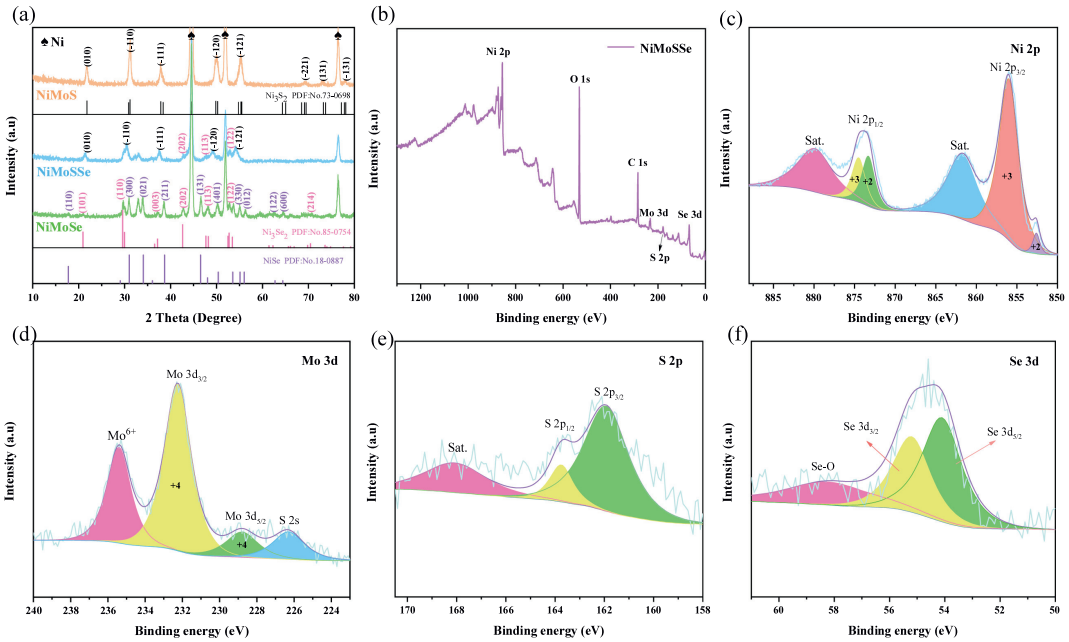

Fig. 1. Structure characterization: (a, b) XRD patterns. (c-f) XPS spectra.

X-ray diffraction analyzer (XRD, Shimadzu-7000, Cu Kα) was used to characterize the crystal structure of the samples. The surface chemical states of elements were investigated by X-ray photoelectron spectrum (XPS, ESCALAB250). The microstructures of the samples were observed by scanning electron microscope (SEM, Gemini, 300-71-31). Finally, we studied pore size and specific surface area of the sample by Brunauer-Emmett-Teller (BET, Micromeritics ASAP) method.

The electrochemical performances of the samples were performed in an electrochemical work station (Shanghai Chenhua CHI600E) in 3 mol/L KOH electrolyte. The as-prepared product was used as working electrode, Hg/HgO electrode and Pt foil were served as the reference and counter electrodes, respectively. The specific capacitance, energy density and power density of the electrodes are calculated by the following formulas:

$$C = I\Delta t/m \tag{1}$$

$$E = 1/2CV^2 \tag{2}$$

$$P = 3600E/t \tag{3}$$

where C, I, t, m, E, V and P represent specific capacitance, current, discharge time, the mass of cathode, energy density, potential window and power density, respectively.

The assembled asymmetric supercapacitor consists of a positive electrode, a negative electrode, electrolyte and separator. NiMoSSe samples and AC were used as anode and cathode, respectively. Activated carbon, carbon black and PVDF were dispersed into *N*-methyl-2-pyrrolidone with the ratio of 7:2:1. The negative electrode was obtained by uniformly coating the above slurry on the pretreated nickel foam. The optimal mass ratio of electrode materials can be determined by the following equation:

$$m^+/m^- = C^-\Delta V^-/(C^+\Delta V^+) \tag{4}$$

where m, C, V stand for loading mass, mass capacitance and voltage window, respectively.

Firstly, we study the phase structural of the samples. Three obvious diffraction peaks at 44.5°, 51.8° and 76.4° are attributed to Ni phase (JCPDS No. 87-0712), which can be seen from Fig. 1a. The NiMoS samples are synthesized without adding Se element, and several definite diffraction peaks appear at 21.81°, 30.89°, 37.89°, 49.85° and 55.3°, which can well match with the (010), (110), (111), (120) and (-121) crystal planes of Ni_3S_2 phase (JCPDS No. 73-0698). Similarly, NiMoSe samples are also prepared without adding S element, and the peak signals are indexed to the structures of Ni_3Se_2 (JCPDS No. 85-0754) and NiSe (JCPDS No. 18-0887). It can be clearly observed that the diffraction peaks of NiMoSSe samples are consistent with Ni_3S_2 and Ni_3Se_2 phases, and there are no other peaks, which proves its excellent crystallinity. In addition, we donot observe the existence of MoS_2 and $MoSe_2$ phases because the content is lower than the detection limit of XRD [26].

From XPS survey spectra (Fig. 1b), the NiMoSSe sample is composed of Ni, Mo, S and Se elements. The Ni 2p spectra (Fig. 1c) can be fitted with two spin-orbit peaks of Ni $2p_{3/2}$ and Ni $2p_{1/2}$ accompanied with two satellite peaks. The binding energies of 873.3/852.6, 874.5/856, and 879.9/861.7 eV are assigned to Ni^{2+}, Ni^{3+} and two "Sats.", respectively [27]. In Mo 3d spectra (Fig. 1d), the peaks with binding energies at 232.25 eV and 228.8 eV are attributed to Mo $3d_{3/2}$ and Mo $3d_{5/2}$ [28]. It can be found that the peak at 235.4 eV is associated with Mo^{6+}, which is due to the partial oxidation of unsaturated Mo atoms [29]. The fitted peak at 226.3 eV is indexed to the binding energy of S 2s of MoS_2 [30]. Fig. 1e shows the high-resolution S 2p spectra. It contains S $2p_{1/2}$ and S $2p_{3/2}$ orbits, which are located at 163.75 eV and 161.93 eV, respectively [31]. Moreover, the peak at 168.08 eV corresponds to a shake-up satellite. The Se 3d spectra of the sample is depicted in Fig. 1f, two peaks at 55.2 eV and 54.1 eV can be ascribed from Se $3d_{3/2}$ and Se $3d_{5/2}$ [32]. Based on the above results, it is confirmed that the presence of MoS_2 and $MoSe_2$ in NiMoSSe material.

From Figs. 2a and d, NiMoS samples show uneven spherical structures with an average diameter of 350 nm. It is found that many thin nanosheets are grown on the surface of NiMoS nanospheres to obtain NiMoSSe materials (Figs. 2b and e). The abundant mesopores on the surface are not completely covered by

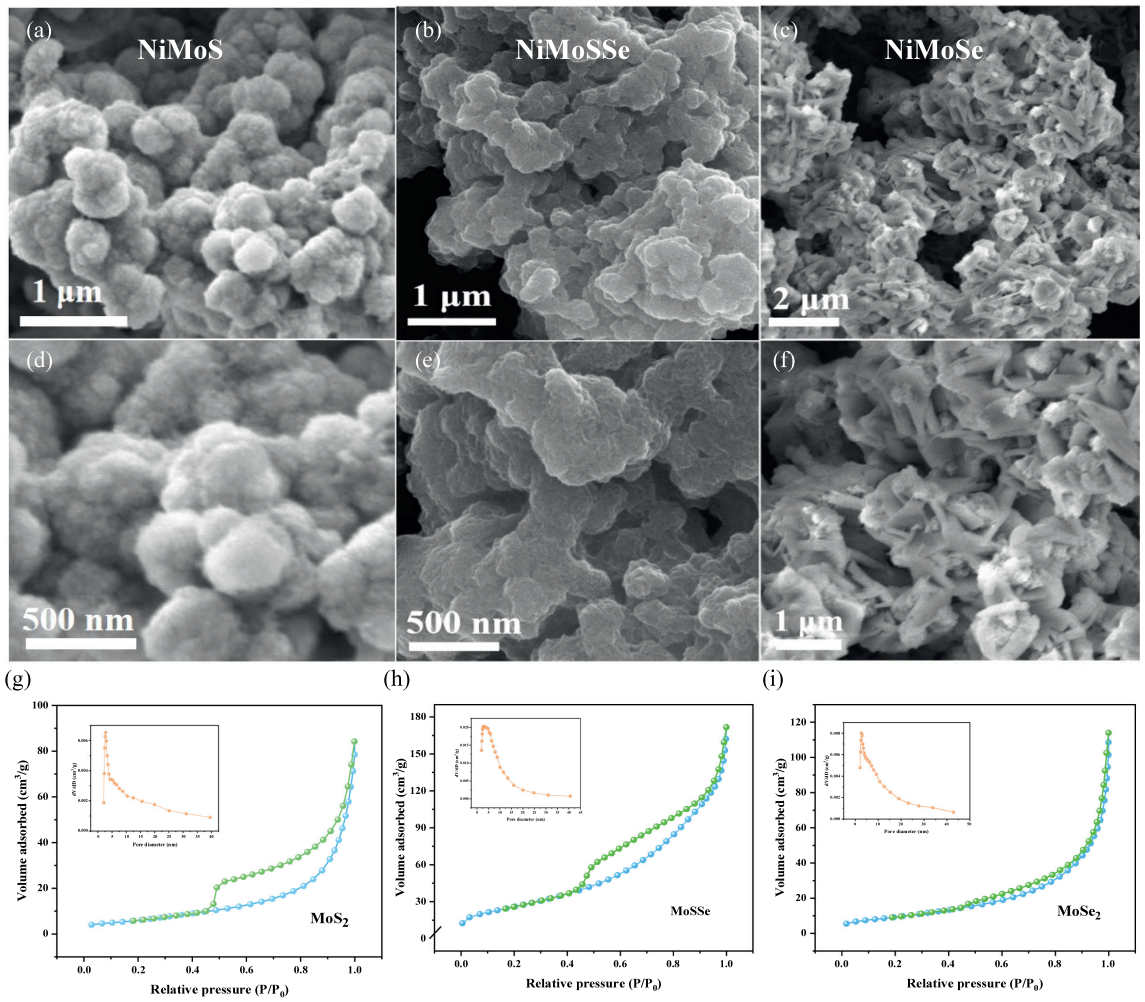

Fig. 2. Morphology characterization: The SEM images of (a, d) NiMoS, (b, e) NiMoSSe, and (c, f) NiMoSe. (g-i) N_2 adsorption-desorption isotherm of samples, the inset shows the pore size distribution.

disordered nanosheets. It promotes the penetration speed of electrolyte and creates effective channels for ion transfer. It can be seen from Figs. 2c and f that NiMoSe samples exist in the form of irregular nano-flakes. Studies show that nanosheets possess high specific surface area and suitable porosity, which provide abundant paths for ions transport. Figs. 2g-i present the isothermal adsorption and desorption curves of the samples, and the pore size distributions are shown in the insets. The specific surface area of MoS_2, MoSSe and $MoSe_2$ are 25.18, 98.56 and 36.28 m^2/g, respectively. The specific surface area of MoSSe composite is much larger than those of pure MoSe and MoS samples. Meanwhile, it shows outstanding electrochemical activity during redox reaction and promote the entry of ions at the electrode/electrolyte interface.

Fig. 3a shows the CV curves of three samples with a pair of obvious redox peaks. It indicates that their energy storage process is mainly controlled by Faraday redox reaction. Compared with the other two samples, NiMoSSe electrode possesses more prominent redox signal peak and larger integration area. It implies that its specific capacitance is greatly optimized owing to the synergistic effect between bimetallic (S/Se) ions. Fig. 3b indicates the constant current charge-discharge (GCD) curves of the electrodes at 1 A/g. All the curves maintain a stable voltage platform. The specific capacitance of NiMoSSe (1035 C/g) is larger than those of NiMoS (614 C/g) and NiMoSe (690 C/g) samples. Its excellent electrochemical performance is mainly attributed to the unique surface structure. It can reduce the capacitance drop caused by volume expansion and improve the utilization rate of active materials.

Impedance measurement is also an important method to evaluate the performance of electrode materials. For the Nyquist diagram of an ideal supercapacitor, a semicircle related to the charge transfer impedance can be observed in the high frequency region. And a vertical line appears in the low frequency region. In fact, the actual electrode behavior is more complicated than the ideal state owing to the factors such as dispersion. As usual, a semicircle and a straight line with a certain slope appear in the high and low frequency region, respectively. As shown in Fig. 3c, NiMoSSe electrode presents a relatively small semicircular diameter compared with NiMoS and NiMoSe materials. This material shows a low charge transfer resistance (R_{ct}), indicating that its outstanding charge transfer kinetics. Fig. 3d depicts that the capacitance decreases with the increase of current density. NiMoSSe electrode can still provide a specific capacitance as high as 668 C/g even at 10 A/g. It can be seen from Fig. 3e that the NiMoSSe material belongs to a typical battery-type electrode material. Cyclic stability experiments of three electrode materials are conducted at 10 A/g (Fig. 3f). The NiMoSSe sample maintains 79.86% of the initial capacity, demonstrating its excellent electrochemical performance.

To further investigate the practical application of the prepared samples, several asymmetric supercapacitors are assembled using NiMoSSe sample and activated carbon (AC) as electrodes. The CV

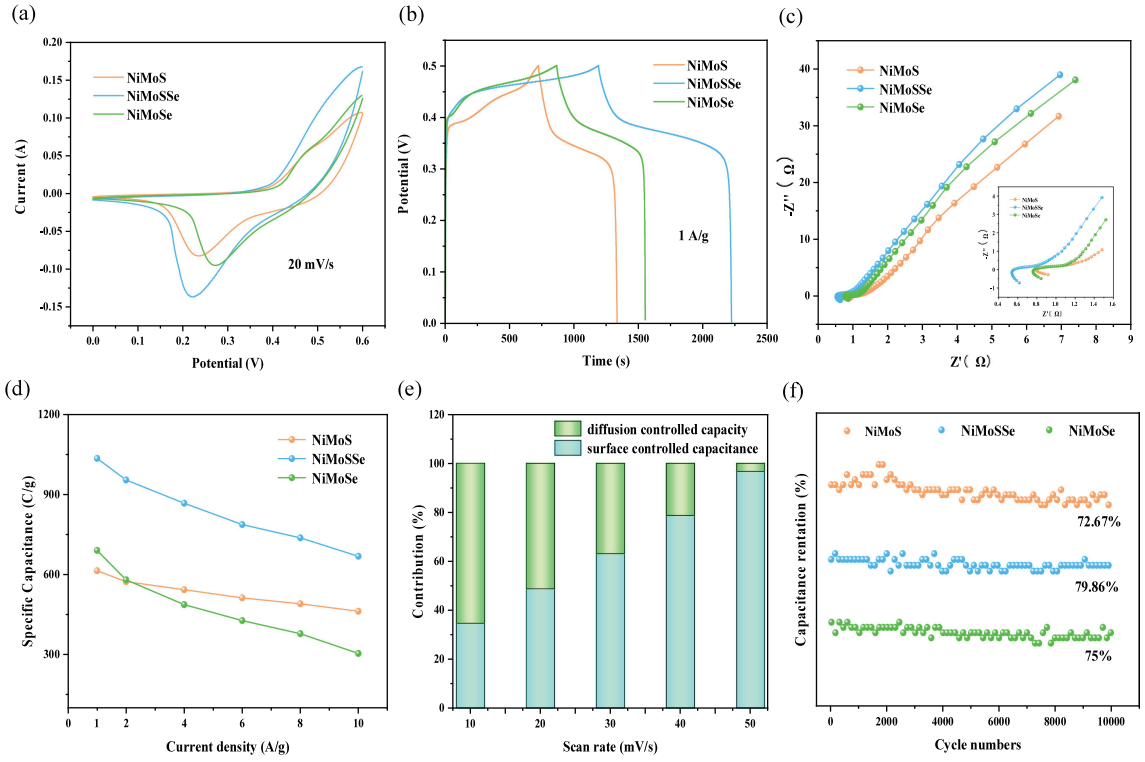

Fig. 3. Electrochemical performance: (a) CV curves. (b) GCD curves. (c) Nyquist plots. (d) Specific capacitance at various current densities. (e) Contribution ratio between surface and diffusion-controlled capacitances. (f) Cycling performance.

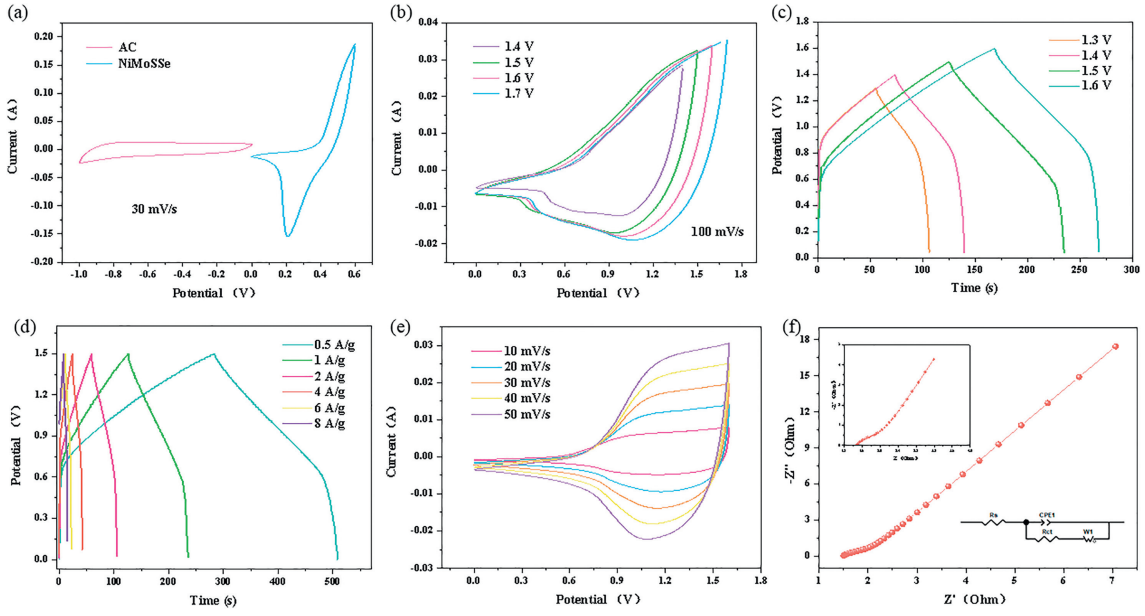

Fig. 4. Electrochemical performance of asymmetric device: (a) CV curves of anode and cathode. (b, c) CV and GCD curves in different voltage windows. (d) GCD curves at various current densities. (e) CV curves at different scanning speeds. (f) Nyquist plots.

curves (Fig. 4a) show that the working voltage windows of AC and NiMoSSe electrodes are -1∼0 V and 0∼0.6 V, respectively. It implies that ASC device can work stably at 1.6 V. A series of CV curves in different voltage windows are performed at 100 mV/s (Fig. 4b). We observe no obvious polarization phenomenon, which further proves that the stable voltage window of ASC. The GCD curves of the device are kept well in different voltage windows, revealing its excellent stability (Fig. 4c). Fig. 4d shows the relationship between the capacitance of devices and the current density. The specific capacitance is 75.24 F/g at 0.5 A/g, and when it increases to 2 A/g, it is still as high as 63.08 F/g. As shown in Fig. 4e, when the scanning speed increases, the integral area of CV curve also increases. It proves the typical reversible Faraday pseudo-capacitance behavior during redox reaction. In addition, we find that the CV curves at different scanning speeds do not show obvious shape distortion, which indicates that the porous structure promote the rapid ions

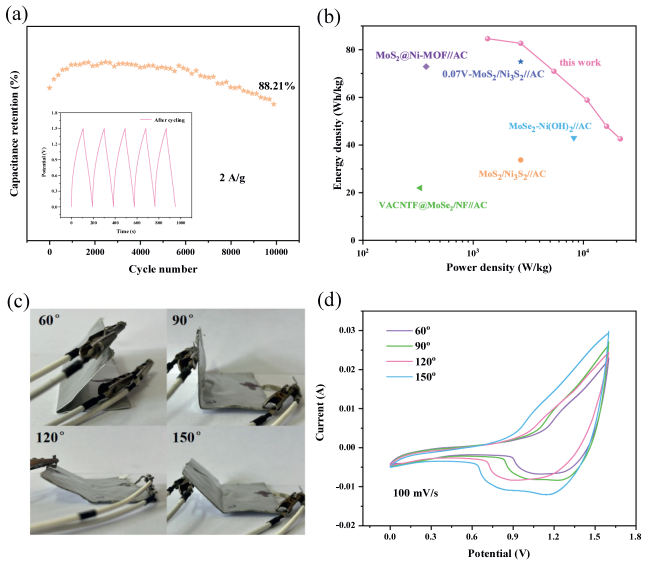

Fig. 5. (a) Cycling performance. (b) Ragone plots. (c) Electrode pictures at different bending angles. (d) CV curves of the electrode after bending.

migration. From EIS curve, the device possesses low charge transfer resistance (1.49 Ω) in high frequency region (Fig. 4f), which further proves the outstanding rate performance of NiMoSSe//AC ASC.

Fig. 5a indicates the cycling performance of the device at 2 A/g. We can observe that the specific capacitance is continuously activated in the first 1000 cycles, and then begin to decay. The device only loses 11.79% of its initial capacity after 10000 cycles. Fig. 5b shows the Ragone plot of NiMoSSe//AC and several hybrid devices [33–37]. It demonstrates that its energy density and power density are obviously higher than those of other materials (82.71 Wh/kg at 2700 W/kg, 42.6 Wh/kg at 21600 W/kg). Finally, the mechanical property of the device is studied under different bending angles. Fig. 5c is the photo of bending devices. It is found that the shapes of CV curves remain unchanged (Fig. 5d), which proves its outstanding stability.

In summary, we have synthesized NiMoSSe composites through a facile hydrothermal route. The obtained product possesses excellent electronic conductivity, rate performance and high specific capacitance. Moreover, the interaction between active components reduces the electrochemical stress generated during charging and discharging, which is beneficial to the rapid redox reaction. This makes NiMoSSe sample show large specific surface area and abundant active sites. This rational design also prevents the structural collapse of electrode materials and maintains the superior stability after long cycles. It suggests that the prepared electrode materials can be used for the development of energy storage devices with high power density and energy density.

Declaration of competing interest

The authors declare that they have no known competing financial interests or personal relationships that could have appeared to influence the work reported in this paper.

Acknowledgment

The work is supported by National Natural Science Foundation of China (No. 52172218).

References

[1] Y. Liu, Y. Liu, Xiang Wu, Chin. Chem. Lett. 34 (2023) 107839.
[2] Y.M. Wang, X.L. Wu, Y.Q. Han, T.X. Li, J. Energy Storage 42 (2021) 103053.
[3] M.D. Wang, X.Y. Liu, X. Wu, Nano Energy 114 (2023) 108681.
[4] Q.C. Zhu, D.Y. Zhao, M.Y. Cheng, et al., Adv. Energy Mater. 9 (2019) 1901081.
[5] H.Q. Liu, D.P. Zhao, M.Z. Dai, et al., Chem. Eng. J. 428 (2022) 131183.
[6] X.W. Wang, Y.C. Sun, W.C. Zhang, X. Wu, Chin. Chem. Lett. 34 (2023) 107593.
[7] Y. Liu, P.F. Hu, H.Q. Liu, et al., Inorg. Chem. Front. 6 (2019) 2824–2831.
[8] P. Hao, Z.H. Zhao, Y.H. Leng, et al., Nano Energy 15 (2015) 9–23.
[9] Q. Xia, T. Xia, X. Wu, Rare Metal 41 (2022) 1195–1201.
[10] Z.Y. Gao, C. Chen, J.L. Chang, et al., Chem. Eng. J. 343 (2018) 572–582.
[11] H.Q. Liu, M.Z. Dai, D.P. Zhao, X. Wu, ACS Appl. Energy Mater. 3 (2020) 7004–7010.
[12] X.M. Geng, Y.L. Zhang, Y. Han, et al., Nano Lett. 17 (2017) 1825–1832.
[13] T.Y. Wang, S.Q. Chen, H. Pang, H.G. Xue, Y. Yu, Adv. Sci. 4 (2017) 1600289.
[14] X.L. Chen, T. Shi, K.L. Zhong, G.L. Wu, Y. Lu, Chem. Eng. J. 379 (2020) 122240.
[15] M. Acerce, D. Voiry, M. Chhowalla, Nat. Nanotechnol. 10 (2015) 313–318.
[16] X. Wang, H. Li, H. Li, et al., Adv. Funct. Mater. 30 (2020) 0190302.
[17] N. Joseph, P.M. Shafi, A.C. Bose, Energy Fuel 34 (2020) 6558–6597.
[18] S. Mishra, P.K. Maurya, A.K. Mishra, Mater. Chem. Phys. 255 (2020) 123551.
[19] C.M. Yang, L.H. Zhou, Y.C. Liang, Appl. Catal. B: Environ. 304 (2022) 120993.
[20] H.W. Huang, J. Cui, L. Zhang, ACS Nano 13 (2019) 3448–3456.
[21] E.Z. Xu, Y. Zhang, Y. Jiang, Chem. Eng. J. 385 (2020) 123839.
[22] Y.Y. Wang, W.P. Kang, X.J. Pu, et al., Nano Energy 93 (2022) 106897.
[23] S.V.P. Vattikuti, K.C. Devarayapalli, P.C. Nagajyothi, J. Shim, Microchem. J. 153 (2020) 104446.
[24] X. Zhao, W. Cai, Y. Yang, et al., Nano Energy 47 (2018) 224–234.
[25] S.Z. Li, W.J. Zang, X.M. Liu, et al., Chem. Eng. J. 359 (2019) 1419–1426.
[26] Y. Liu, D.P. Zhao, H.Q. Liu, A. Umar, X. Wu, Chin. Chem. Lett. 30 (2019) 1105–1110.
[27] X.H. Guan, M. Huang, L. Yang, G.S. Wang, X. Guan, Chem, Eng. J. 372 (2019) 151–162.
[28] J.G. Ju, L.T. Zhang, H.S. Shi, et al., Appl. Surf. Sci. 484 (2019) 392–402.
[29] M.A. Bissett, I.A. Kinloch, R.A.W. Dryfe, ACS. Appl. Mater. Inter. 7 (2015) 17388–17398.
[30] N. Chen, C.P. Han, R.Y. Shi, et al., Electrochim. Acta 283 (2018) 36–44.
[31] X. Zheng, Y.K. Deng, Y.L. Wang, et al., New Carbon Mater. 33 (2019) 554–561.
[32] Y.Q. Zhang, H.C. Tao, S.L. Du, X.L. Yang, ACS Appl. Mater. Interfaces 11 (2019) 11327–11337.
[33] J.X. Liu, X. Wu, J. Solid State Electrochem. 27 (2023) 2571–2577.
[34] B. Kirubasankar, P. Palanisamy, S. Arunachalam, V. Murugadoss, S. Angaiah, Chem. Eng. J. 355 (2018) 881–890.
[35] L.G. Yue, X. Wang, T.T. Sun, et al., Chem. Eng. J. 375 (2019) 121959.
[36] Y.H. Liu, W.L. Li, X.W. Chang, et al., J. Colloid Interf. Sci. 562 (2020) 483–492.
[37] J.X. Liu, S.Q. Zhao, A. Umar, X. Wu, Mater. Today Sustain. 23 (2023) 100433.